

## *Solar Dynamics Observatory and Hinode* Observations of a Blowout Jet in a Coronal Hole

P.R. Young<sup>1</sup> · K. Muglach<sup>2,3</sup>

© Springer ●●●

**Abstract** A blowout jet occurred within the south coronal hole on 9 February 2011 at 09:00 UT and was observed by the *Atmospheric Imaging Assembly* (AIA) and *Helioseismic and Magnetic Imager* (HMI) onboard the *Solar Dynamics Observatory*, and the *EUV Imaging Spectrometer* (EIS) and *X-Ray Telescope* (XRT) onboard the *Hinode* spacecraft during coronal hole monitoring performed as part of *Hinode* Operations Program No. 177. Images from AIA show expanding hot and cold loops from a small bright point with plasma ejected in a curtain up to 30 Mm wide. The initial intensity front of the jet had a projected velocity of 200 km s<sup>-1</sup> and line-of-sight (LOS) velocities measured by EIS are between 100 and 250 km s<sup>-1</sup>. The LOS velocities increased along the jet, implying an acceleration mechanism operating within the body of the jet. The jet plasma had a density of  $2.7 \times 10^8$  cm<sup>-3</sup> and a temperature of 1.4 MK. During the event a number of bright kernels were seen at the base of the bright point. The kernels have sizes of  $\approx 1000$  km, are variable in brightness, and have lifetimes of 1–15 minutes. An XRT filter ratio yields temperatures of 1.5–3.0 MK for the kernels. The bright point existed for at least ten hours, but disappeared within two hours after the jet, which lasted for 30 minutes. HMI data reveal converging photospheric flows at the location of the bright point, and the mixed-polarity magnetic flux canceled over a period of four hours on either side of the jet.

**Keywords:** Coronal holes; Jets; Magnetic Fields, photosphere; Spectral Line, Intensity and Diagnostics; Spectrum, Ultraviolet; Velocity Fields, Photosphere

### 1. Introduction

Solar jets are recognized in image sequences as dynamic structures that yield a narrow, columnar structure extending away from the solar surface. Coronal holes present particularly favorable locations for studying coronal jets due to the low

---

<sup>1</sup> College of Science, George Mason University, 4400 University Drive, Fairfax VA 22030, USA  
email: pyoung9@gmu.edu

<sup>2</sup> Code 674, NASA Goddard Space Flight Center, Greenbelt, MD 20771, USA  
email: kmuglach@gmx.de

<sup>3</sup> ARTEP, Inc., Ellicott City, MD 21042, USA

intensity of the background corona. Surveys of coronal hole jets performed by Nisticò *et al.* (2009) and Moore *et al.* (2010) have identified different types of jets and, in particular, one type that appears similar to a coronal mass ejection (CME) although on a much smaller spatial scale. An example of this type of event is presented here, uniquely combining coronal spectroscopic data from the *EUV Imaging Spectrometer* (EIS: Culhane *et al.*, 2007) onboard the *Hinode* spacecraft (Kosugi *et al.*, 2007), and high-cadence, high-spatial resolution data from the *Atmospheric Imaging Assembly* (AIA: Lemen *et al.*, 2012) and *Helioseismic and Magnetic Imager* (HMI: Scherrer *et al.*, 2012) onboard the *Solar Dynamics Observatory* (SDO).

Nisticò *et al.* (2009) performed a survey of coronal hole jets observed with the *Sun Earth Connection Coronal and Heliospheric Investigation* (SECCHI) instruments on the two *Solar Terrestrial Relations Observatory* (STEREO) spacecraft, and five of the 79 events were considered to be small versions of coronal mass ejections dubbed “micro-CMEs”. Such events were identified as having a three-part structure of bright leading edge, dark void, and bright trailing edge in analogy to the structures seen when CMEs are viewed at the limb. Note that two of the five events demonstrated a helical structure.

A survey of jets observed with the *X-Ray Telescope* (XRT: Golub *et al.*, 2007) onboard the *Hinode* spacecraft was performed by Moore *et al.* (2010) who categorized jets as “standard” or “blowout”. The standard jets are the equivalent of the categories “lambda” and “Eiffel Tower” used by Nisticò *et al.* (2009), while blowout jets are the equivalent of the micro-CME jets of Nisticò *et al.* (2009). Moore *et al.* (2010) defined a blowout jet to be one in which the base arch of the bright point is blown open during the event, whereas the arch remains closed for standard jets. (The base arch is an X-ray bright loop structure that spans the base of the jet.) By inspecting cooler images from the EUVI instruments onboard the STEREO spacecraft for some of the events, Moore *et al.* (2010) concluded that the blowout jets also exhibit the expulsion of cool material.

In the present article we will present photospheric magnetic field, and coronal spectroscopic and imaging data for a blowout jet. The magnetic evolution of jets has been previously discussed and a key result is that convergence and cancellation of magnetic elements are commonly associated. For example, Wang *et al.* (1998) found that 80% of  $H\alpha$  jets in quiet solar regions are associated with converging magnetic dipoles, while Chifor *et al.* (2008) found that an active region coronal jet was associated with repeated flux cancellation. Two examples of coronal jets at a coronal hole boundary were presented by Yang *et al.* (2011), both identified with flux cancellation. A survey of the magnetic signatures of X-ray brightenings within a coronal hole observed with the *Solar Optical Telescope* (SOT: Tsuneta *et al.*, 2008) and XRT onboard *Hinode* was presented by Huang *et al.* (2012) who found that all of the 22 X-ray brightenings were associated with canceling flux. One of these events was a jet. Flux cancellation was also observed in many cases of transition region explosive events by Muglach (2008). An event described as a standard-to-blowout jet exhibited flux emergence, convergence, and cancellation in observations presented by Liu *et al.* (2011).

There have been several spectroscopic studies of coronal hole jets with EIS, and we focus on those for which velocity measurements for the plasma within the

jet (rather than the bright point) were made, as this is the measurement made in the present article. Kamio *et al.* (2007) found line-of-sight (LOS) blueshifts of about  $30 \text{ km s}^{-1}$  in the He II  $256.3 \text{ \AA}$  and Fe XII  $195.1 \text{ \AA}$  emission lines for one jet observed just inside the solar limb. A coronal background subtraction however, such as performed in the present article, may have led to higher velocities. A subsequent study by Kamio *et al.* (2009) did perform two Gaussian fits to two separate jets observed in Fe XII  $195.1 \text{ \AA}$ , yielding LOS velocities of  $-50$  and  $-96 \text{ km s}^{-1}$  for the jet plasma. A jet observed by Doschek *et al.* (2010) showed LOS velocities of  $\approx -15$  to  $-20 \text{ km s}^{-1}$ , although this is again the Doppler shift of the combined background plus jet emission line profile. Doschek *et al.* (2010) also derived temperatures of  $1.1\text{--}1.3 \text{ MK}$  in the jet and densities of  $5\text{--}70 \times 10^7 \text{ cm}^{-3}$ .

A detailed study of a bright jet in a low latitude coronal hole was performed by Madjarska (2011). LOS velocities within the broad jet ranged from  $-30$  to  $-150 \text{ km s}^{-1}$ , although for a small region at one side of the jet a clear two component structure to the emission lines could be identified. Just above the bright point the velocity of this component was  $-310 \text{ km s}^{-1}$ , decreasing to  $-150 \text{ km s}^{-1}$  over a projected distance of about  $10 \text{ Mm}$  (measurements made in Fe XII  $195.1 \text{ \AA}$ ). This high-velocity component was seen over a wide range of temperatures, from  $0.5 \text{ MK}$  to  $2.0 \text{ MK}$ .

Section 2 summarizes the types of observations used in the present article, and Section 3 gives an overview of the event. Section 4 discusses the evolution of the bright point that gives rise to the jet, and Section 5 discusses the jet itself. A summary of the results is given in Section 6. For the remainder of this article we will refer to the event as a blowout jet.

## 2. Observations

The *Hinode* observations discussed here were obtained through *Hinode* Observing Program No. 177 (HOP 177), entitled “Magnetic structures within coronal holes” (PI: P.R. Young). Observations were obtained during 8–10 February 2011 when the south polar hole had an equatorial extension, perhaps related to active region AR 11156, which lay at the north boundary of the coronal hole. A number of distinctive features were identified in line-of-sight (LOS) velocity images obtained from the Fe XII  $195.12 \text{ \AA}$  emission line, the majority of which were identified to be jets. A summary of these jet observations will be given in a future publication, and the present article focuses on one of the jets, which is classed as a blowout jet. The major evolution of the jet and associated bright point occurred between 08:45 and 09:20 UT on February 9.

EIS captured the jet with a raster that began at 09:05 UT on 9 February 2011. The raster scanned an area of  $179'' \times 512''$  with a 60-second exposure time at each slit position, giving a raster duration of 62 minutes. Many emission lines were observed although this article principally focuses on Fe XII  $195.12 \text{ \AA}$  (formed at  $1.5 \text{ MK}$ ). The EIS data were calibrated using the standard options recommended in the EIS data-analysis guide ([solarb.mssl.ucl.ac.uk:8080/eiswiki/Wiki.jsp?page=EISAnalysisGuide](http://solarb.mssl.ucl.ac.uk:8080/eiswiki/Wiki.jsp?page=EISAnalysisGuide)).

and Gaussian fitting of the emission lines was performed using software described by Young (2012).

XRT obtained images in the Be-thin and Ti-poly filters at approximately 150-second cadence, however there is a data gap between 09:03 and 09:25 UT. Note that two Ti-poly exposures with different exposure times are taken for each of the Be-thin exposures. The Be-thin filter has a greater sensitivity to hot plasma than the Ti-poly filter.

The AIA and HMI instruments onboard SDO observe the entire Sun with regular, high temporal cadences and so both instruments captured the evolution of the jet. AIA obtains images in seven EUV filters at 12-second cadence, and two UV filters at 2-second cadence. In this article we use the notation “*A171*”, “*A193*”, *etc.*, to refer to the AIA filters centered at 171 and 193 Å. HMI takes polarized full disk images with two camera systems: the front camera measures the Stokes-*I* and -*V* parameters only and the data pipeline yields LOS magnetograms, Dopplergrams and intensity images at a 45-second cadence; the side camera measures all four Stokes parameters to allow the full vector magnetic field to be computed at a 720-second cadence. The data pipeline for the side camera also yields LOS magnetograms at a 720-second cadence, which have a somewhat higher sensitivity than the front camera 45-second magnetograms (Liu *et al.*, 2012). Both types of LOS magnetograms are used in the present article.

Calibration software for all datasets was obtained from the IDL SolarSoft library ([www.lmsal.com/solarsoft/](http://www.lmsal.com/solarsoft/)). For all images shown in this article, the listed time corresponds to the midpoint of the exposure, given in Coordinated Universal Time (UTC) format. Three movies created from *A193* data and one from HMI data are presented in the following sections. Additional movies for the event, generated from XRT, HMI, and other AIA filters, are available at [pyoung.org/jets/hop177/jet\\_27.html](http://pyoung.org/jets/hop177/jet_27.html).

### 3. Event Overview

Jets were identified in the coronal hole by fitting a single Gaussian function to the Fe XII 195.12 Å emission line and constructing line-of-sight Doppler velocity maps from each EIS raster. The blowout event presented here showed the largest Doppler signatures of all the jets identified from the dataset. Figure 1 shows the discovery image together with intensity and line width images. EIS rasters from right to left and the images shown in Figure 1 were obtained from 09:06 to 09:36 UT. The first eight exposures were badly affected by particle hits during a South Atlantic Anomaly encounter; thus the first useful exposure was at 09:14 UT. The bright point at the base of the event was observed between 09:21 and 09:29 UT.

The intensity image from Figure 1 shows a faint, narrow structure coming from the small bright point in the top-left of the raster but otherwise is not distinctive. The velocity and line width images, however, show a very clear structure: a thick column (observed between 09:14 and 09:18 UT) with a short, narrow leg that connects to the bright point.

Movie 1 shows a sequence of *A193* images at one-minute cadence with the field-of-view cropped to show the jet and the bright point. The movie covers the

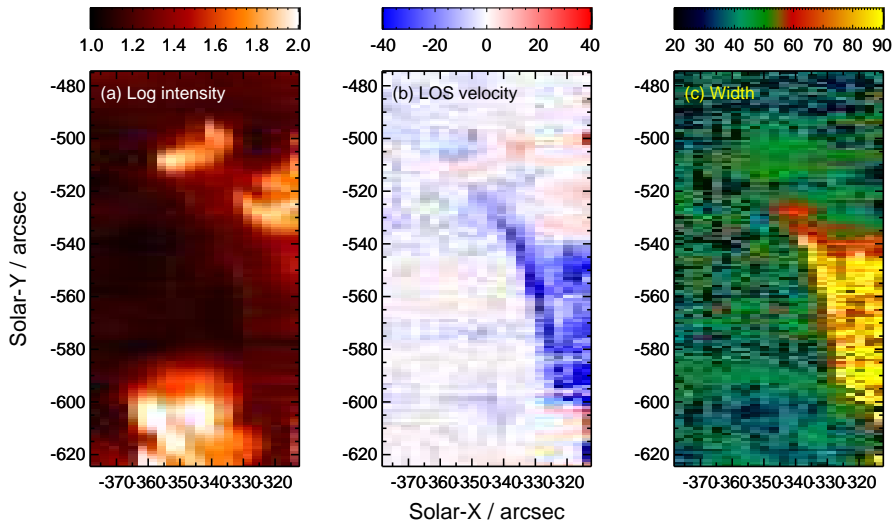


**Figure 1.** Images of the jet derived from single Gaussian fits to the Fe XII 195.12 Å emission line observed by EIS. The left panel shows the logarithm of intensity in units  $\text{erg cm}^{-2} \text{s}^{-1} \text{sr}^{-1}$ , the middle panel shows LOS velocities in  $\text{km s}^{-1}$ , and the right panel shows line width in mÅ. The instrumental line width has been removed.

period 08:30 to 09:39 UT, and it shows expanding loops coming from the bright point in the top-left of Figure 1 over the period 08:50 to 08:59 UT with a wide jet becoming prominent between 09:00 and 09:23 UT. The jet expands laterally and fades over this time period. The shape of the jet in the EIS velocity image (Figure 1b) matches the shape of the  $A193$  structure. Note that the EIS velocity signature is much more prominent than the  $A193$  intensity structure.

The long-term evolution of the jet's bright point was studied with HMI 720-second LOS magnetograms and 12-minute cadence  $A193$  images obtained over the period 03:00 to 12:00 UT. The HMI 720-second magnetograms show positive and negative polarities separated by about  $10''$  at 03:00 UT. They come towards each other until they are separated by  $2-3''$  and seem to annihilate each other between 09:00 and 10:00 UT. Figure 2 shows six HMI images during the evolution of the bright point and also the variation of the unsigned magnetic flux with time. The magnetic flux was averaged over a  $22'' \times 25''$  region containing the strong magnetic polarities, and a background level obtained by averaging over a wider  $60'' \times 60''$  field of view was subtracted. The dotted line on Figure 2g shows the variation of the  $A193$  intensity averaged over a  $40'' \times 37''$  region containing the bright point. A background value obtained from a nearby dark region within the coronal hole was subtracted.

Figure 2 shows that magnetic cancellation began at around 07:30 UT and continued until the average flux reached background levels at 11:00 UT. The  $A193$  intensity also falls over this period, although there are three short episodes of intensity increases, one of which immediately precedes the EIS raster scan of the event (indicated by parallel vertical lines in Figure 2g). The two other

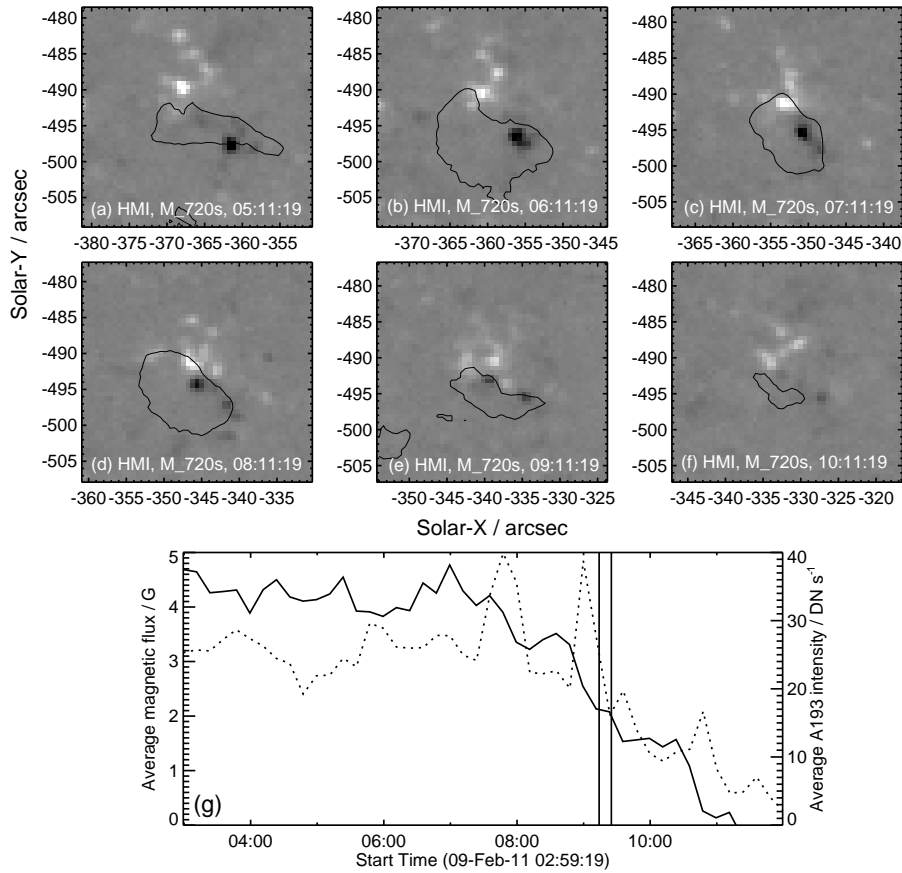


**Figure 2.** Panels a to f show HMI 720-second magnetograms at six different times. The magnetic flux has been saturated at  $\pm 200$  G in each image. The contours show an  $A193$  intensity level of  $100 \text{ DN s}^{-1}$ . Panel g shows the variation of unsigned magnetic flux (solid line) and  $A193$  intensity (dotted line) as a function of time. Background levels have been subtracted for each quantity.

intensity increases did not give rise to jet signatures in the  $A193$  filter, and neither was observed by EIS.

The photospheric magnetic field evolution seen in Figure 2 is dominated by flux convergence and eventual cancellation. We use 45-second cadence HMI white-light images to derive velocities perpendicular to the LOS using the Fourier Local Correlation Tracking code (FLCT: Fisher and Welsch, 2008). The correlation is performed on pairs of images separated in time by 9 minutes as the typical lifetimes of granules are 10–15 minutes. In addition, each image is convolved with a Gaussian function of width  $6.4''$  as typical granule sizes are a few arcseconds. (We note that the correlation was carried out with a range of spatial scales, and the results are similar to those presented here.) The flow field was calculated over a time period of two hours, from 08.00 to 10.00 UT, and the field-of-view was centered on the location of the jet's bright point. The

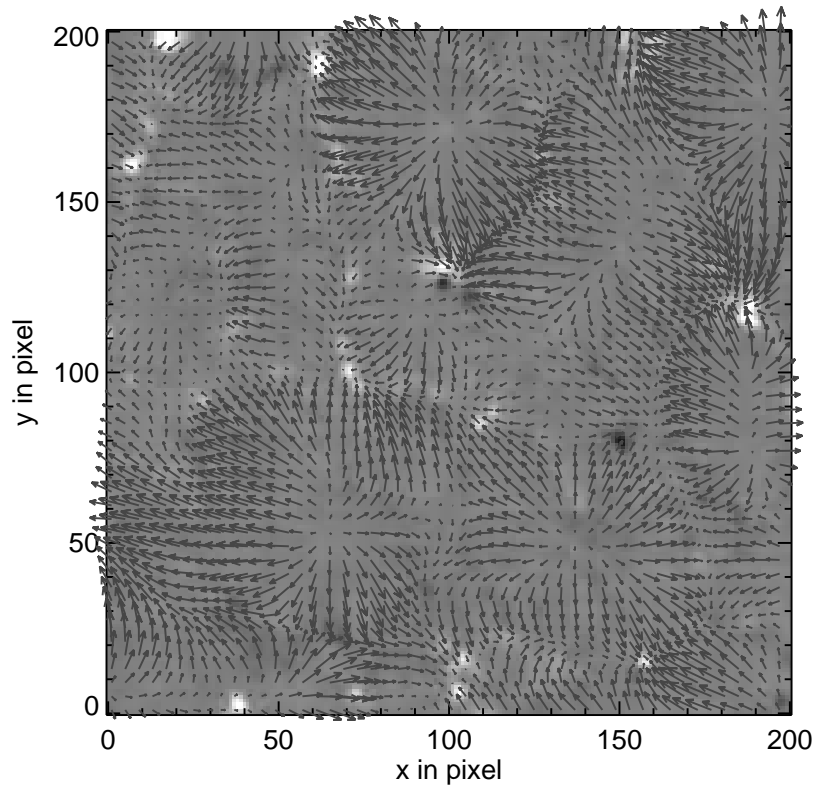


**Figure 3.** A LOS magnetogram averaged over the period 08:00 to 10:00 UT and saturated at a level of  $\pm 100$  G. The jet's bright point is located at (100,130), and a pixel corresponds to  $0.6'' \times 0.6''$ . Arrows show the average plane-of-sky photospheric velocity field, derived from cross-correlating HMI intensity images. The maximum flow-vector magnitude is  $600 \text{ m s}^{-1}$ .

HMI images are filtered to remove the intensity signatures of the solar  $p$ -modes (using a phase velocity of  $3 \text{ km s}^{-1}$ ).

Movie 2 shows the time-resolved flowfield at a 45-second cadence. Figure 3 shows the flow field averaged over two hours to highlight the more persistent flows. The background image of Figure 3 is the time averaged magnetic field, saturated at  $\pm 100$  G, and the jet's underlying bipolar region is at pixel position  $x = 100$ ,  $y = 130$ . The flow field shows the characteristic supergranular patterns with sizes of 20–30 Mm and velocities up to a few hundred  $\text{m s}^{-1}$ . At the jet location one can find the intersection of four supergranules and the flows all converge at this point. The magnetic flux elements found in the coronal hole are therefore swept together leading to the observed flux convergence in the magnetogram sequence. This is followed by flux cancellation as mixed polarities are involved and the observed jet can be considered as the outflow region of the reconnection of the flux system.

Section 4 focuses on the detailed evolution of the bright point during the time period 08:48 to 09:15 UT when the jet was triggered, and Section 5 presents an analysis of the ejected-jet plasma.

#### 4. The Jet’s Bright Point

In this section we describe the changes in the bright point during 08:48 to 09:15 UT, corresponding to the period immediately prior and during the event. (For reference, this is the second narrow intensity peak shown in Figure 2g.) Due to the rapid evolution of features within the bright point we consider the 12-second cadence AIA images, and Movie 3 and Movie 4 show *A193* image sequences, the former with a logarithmic intensity scaling to show better the large scale loops of the bright point, and the latter with a linear scaling to show better the intense brightenings at the bright point base. Individual frames from the *A193* sequence are shown in Figure 4.

In order to relate the evolution of the AIA images to the magnetic field, it is necessary to co-align the AIA and HMI images. For this purpose we consider images taken at around 08:51 UT, which is when an intense, compact brightening is seen at the base of the bright point. This is the first of a number of such brightenings, which we refer to as “kernels” in this article. The kernel is present in the *A1600* image at 08:51:06 UT, but is not present in the *A1700* images around this time. (We attribute this to the kernel emitting strongly in the CIV 1548 and 1550 Å emission lines that contribute to the *A1600* channel.) Now both the *A1600* and *A1700* images show bright points that correspond to small magnetic features in the HMI images, and they can be accurately aligned to HMI. We then cross-correlate the kernel seen in the *A1600* image with that seen in the *A193* image, making the assumption that it is the same feature. This method allows the HMI images to be aligned with the *A193* images, and Figure 4 shows four *A193* images with magnetic field contours overlaid.

Prior to the jet, at 08:48:08 UT (Figure 4a), a small loop-like shape was seen in the *A193* image. If we take into account the location of the bright point on the solar disk, then this loop-like shape can be interpreted as joining the opposite polarities in the magnetic field image. Note that the loop-like shape was spatially offset from the magnetic features by a few arcseconds. We believe that this was because the base of the loop-like shape is obscured by cool material near the solar surface – material that later erupted.

The first activity from the bright point was a single kernel that first appeared at 08:50:20 UT within the dark area underneath the small loop referred to earlier, and Figure 4b shows an image from 08:51:56 UT when the kernel is very intense – at least a factor three brighter than other parts of the bright point. The kernel is about two pixels (900 km) wide in the  $x$ -direction and about five pixels (2200 km) long in the  $y$ -direction. Note that this kernel and some others in the sequence were partially removed by the AIA de-spiking routine (which is intended to remove cosmic rays) and so the routine `AIA_RESPIKE` had to be applied to restore the correct intensity values. (The same procedure also had to be applied to observations of flare kernels by Young *et al.*, 2013.)



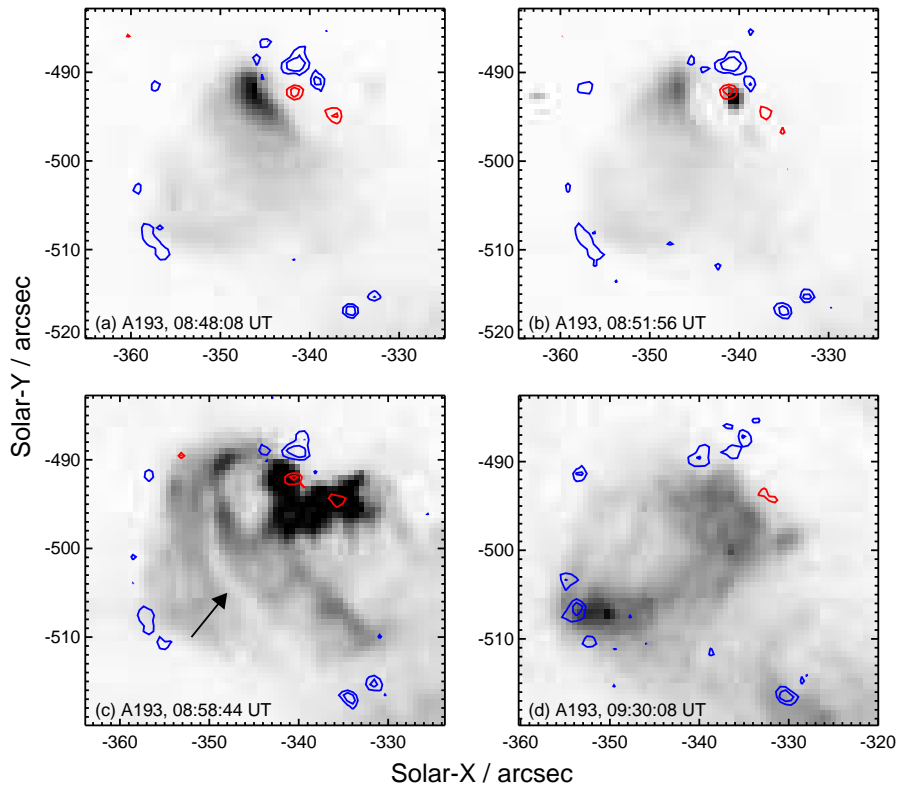


**Figure 4.** Four *A193* images of the bright point that gives rise to the jet. A linear, reversed-intensity scaling is used for each image. The images in panels b and c have been saturated at 500 and 250  $\text{DN s}^{-1}$ , respectively. The actual maxima of the data are 784 and 1064  $\text{DN s}^{-1}$ , respectively. Over-plotted on each image are contours showing the LOS magnetic-field strength, blue representing positive polarity and red negative polarity. The levels shown are 50 and 100 G.

As can be seen from Figure 4b, the initial kernel appears between two small, opposite polarity magnetic features, slightly closer to the negative polarity feature (note that the coronal hole has an overall positive polarity). The location of the kernel is considered accurate due to the fact that the *A1600* image shows both the kernel and the magnetic features, as discussed earlier. The fact that the kernel is very close to the magnetic features is evidence that the kernel is close to the solar surface and not, say, occurring in the corona above the surface.

Inspection of Movie 3 shows that the kernel emits three small jets at 08:51:56, 08:52:56, and 08:54:08 UT. These extend away from the kernel in the southwest direction and fade within about  $10''$  of the kernel's location. After the third jet, the structure at the base of the bright point changes significantly, with multiple kernels appearing along with expanding loop-like shapes and jet structures. Figure 4c shows the appearance at 08:58:44 UT when multiple bright kernels are seen. Note the kernels are arranged between the two negative polarity magnetic

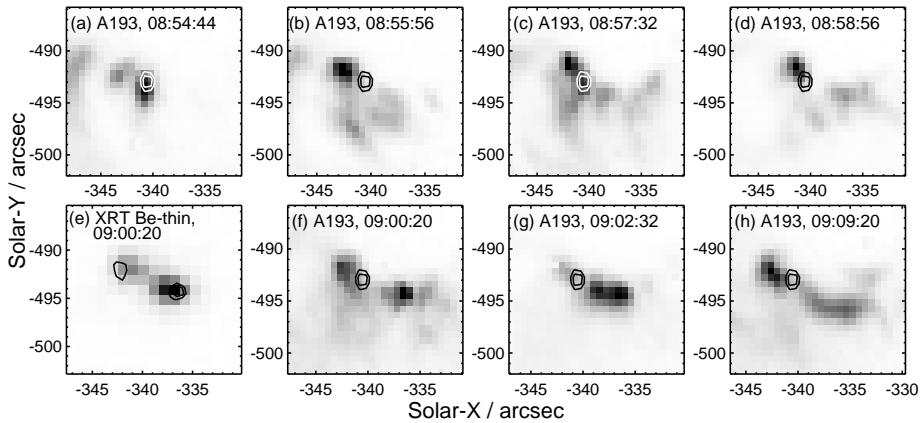


**Figure 5.** Panels a–d and f–h show *A193* images of the kernels within the bright point at different times. On each image contours show the location of the kernel from 08:51:56 UT (Figure 4). Panel e shows a XRT Be-thin image from 09:00:20, the same time as the *A193* image from panel f. The contours on the XRT image show the location of the *A193* kernels from panel f. In each image the color table has been reversed so that black corresponds to a high intensity.

fragments at the bright point base and are not directly connected to the positive polarity fragments.

The full evolution of the kernels in the *A193* filter is best seen in Movie 4, and Figure 5 shows seven snapshots of the kernels at different times. Figure 5 also shows one XRT Be-thin image from 09:00:20 UT (panel 5e) that can be directly compared to an *A193* image from the same time (panel 5f). On each of the *A193* images, contours from the *A193* image at 08:51:56 UT (Figure 4b) are shown in order that the kernels’ positions can be related to the very first kernel. The brightness of the kernels varies in time, so estimating lifetimes is not straightforward. Emission is seen from the location of the first kernel for about eight minutes, while emission is seen from the location of the bright kernel at 08:55:56 UT for about 15 minutes. Significant brightness variations can occur on a frame-by-frame basis (12-second cadence).

A bright-point light curve was obtained by averaging the *A193* emission over the individual image frames of Movie 3 and it reveals one intensity peak between 08:54 and 09:00 UT and another between 09:00 and 09:08 UT (Figure 6). Comparing with Movie 4, the “spikiness” of the first peak is caused by rapid changes in the brightness of the kernels between 08:56 and 08:59 UT. After a brief lull, the kernels brighten again although the variation of intensity in time is more smooth and also the kernels have a more East–West morphology than North–South, perhaps indicating that they are small loops rather than jets in this period. We note also that the two XRT kernels at 09:00:20 UT (Figure 5e) are closer together than the two *A193* kernels at the same time (Figure 5f), which may indicate that the kernels are actually two footpoints of a single, small loop that is hotter at the apex. The variation of the bright point intensity with time is not just driven by the kernels as the larger scale loops expand and brighten, also. The contribution of the non-kernel part of the bright point is greater during

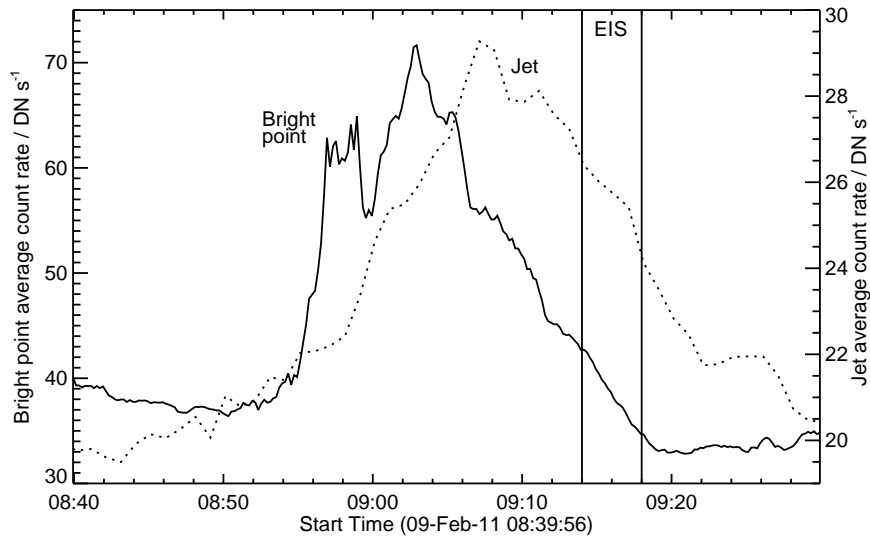


**Figure 6.** *A193* light curves for the bright point (solid line) and a section of the extended jet emission (dotted line). The vertical solid lines indicate the period when EIS scanned the jet.

the second intensity peak. The kernels have largely faded by around 09:10 UT, and by 09:30 UT, when the bright-point intensity has stabilized, the morphology of the bright point has changed significantly (Figure 4d) with loops connecting to a magnetic fragment in the southeast corner of the image being more intense than the initial small loop (Figure 4a).

Considering now the larger scale structure of the bright point, Movie 3 reveals expanding loops that begin rising at around 08:54:00 UT, shortly after the first kernel appeared. An expanding “dark loop” is apparent and is highlighted with an arrow in Figure 4c. From Movie 3 it can be seen that this dark loop initially lay under the small loop shown in Figure 4a. For a loop to appear dark in the *A193* channel it must contain cool material (principally hydrogen and helium) that is absorbing the coronal radiation. The expulsion of cool material during the event is thus consistent with the blowout events studied by Moore *et al.* (2010). In addition to the expanding loops, the movie gives a general impression of outflowing material from the bright point, for example through filamentary structures that disconnect from the kernels and flow outwards.

The temperatures reached during the jet evolution potentially provide an important constraint on the physical mechanism behind the jet. For example, Moreno-Insertis and Galsgaard (2013) find temperatures as high as 7 MK in their model. The temperature within the extended jet feature is discussed in the following section, and here we consider the bright point temperature and, particularly, the temperatures reached in the kernels. Temperatures are best determined with a spectroscopic instrument but unfortunately EIS rastered across the bright point well after the dominant activity within the bright point (Figure 6). Constructing an EIS spectrum of the bright point shows that there is no emission from Fe XVI and only a very weak signal from Fe XV, suggesting a peak temperature of  $< 2$  MK.

The AIA image data potentially allow the kernel temperatures to be measured, but Appendix A demonstrates that differential emission measure curves constructed from the data are not reliable. Instead we use the XRT filter data as the ratio is sensitive to plasma with temperatures  $> 1$  MK. The Ti-poly images are similar to the *A193* images, although there is a greater contrast between the kernels and the more-diffuse bright point and jet emission. The Be-thin filter images show only the kernels, immediately demonstrating that they have a higher temperature than the bright point or jet (since the filter is sensitive to higher temperatures than Ti-poly). The ratio of the filters can yield a temperature, and we take three of the kernels recorded between 08:57 and 09:03 UT, sum their intensities, and compute the intensity ratios. The Be-thin/Ti-poly intensity ratios are 0.05, 0.41, and 0.14 which convert to temperatures of 1.5–3.0 MK (see, *e.g.*, Section 3 of Reeves *et al.*, 2012). We caution that the Be-thin and Ti-poly images were taken 30 seconds apart and the AIA data show that the kernels can evolve on this time-scale, but we do not expect actual temperatures to be significantly different from the stated values.

In summary, the XRT filter-ratio data provide a strong constraint on the maximum temperature in the kernels with values of  $\leq 3$  MK. If there is very hot plasma (10 MK) then the amount is not significant enough to affect the XRT filter ratio measurements.

## 5. The Extended Jet Emission

The jet extending away from the bright point is not a narrow columnar structure but instead is rather broad (a “curtain” in the notation of Moore *et al.*, 2010). The precise width of the jet is difficult to estimate due to contamination by quiet Sun plasma on the west side of the jet, but we estimate that it is approximately  $40''$  (30 Mm). The width increases as the event progresses. In the *A193* images the jet extends about  $120''$  (87 Mm) from the bright point before becoming too faint to see. The jet is clearly not directed in a radial direction, but the east side of the jet is seen to curve towards the Southeast suggesting that the plasma is tending towards a radial direction with height. There is also evidence of fine-scale filamentary structure along the jet’s axis in Movie 1.

The jet is best seen in the *A193* filter, but is also seen in *A171* (dominated by Fe IX) and very weakly in *A131* (which we take to be Fe VIII emission, O’Dwyer *et al.*, 2010). There is no jet emission in *A335*, implying the jet is not hot enough to produce Fe XVI, an ion principally formed over the temperature range 2.2–4.5 MK. As Fe XVI  $335.4 \text{ \AA}$  is a strong transition, this provides a strong constraint for the temperature to be  $\leq 2$  MK independent of the uncertainties of AIA differential emission measure analysis (Appendix A). A movie formed in the *A304* channel does suggest plasma extending above the bright point, consistent with the jet, but it is not clearly seen due to the background coronal hole emission. Movies in these filters are available at [pyoung.org/jets/hop177/jet.27.html](http://pyoung.org/jets/hop177/jet.27.html).

The velocity of the jet in the plane of the sky was estimated by considering *A193* light curves at two different heights. The light curves were derived by averaging the *A193* intensity over  $5 \times 3$  blocks of pixels. By adjusting the position

of the light curve for the greater height to match that for the lower height, the travel time for the jet front could be estimated. Due to the lateral broadening of the jet with time, care was taken to select two locations that brightened during the initial rise of the jet, before the lateral broadening began. We find a projected velocity of  $203 \text{ km s}^{-1}$  at a projected height of 71 Mm above the kernels' location. We estimate an uncertainty of 25% in this measurement due to the noise in the light curves.

Considering a larger portion of the jet, Figure 6 compares the *A193* light curve with that of the bright point (which was discussed in Section 4). The jet light curve was obtained for a  $15'' \times 15''$  region that is within the blue-shifted column of Figure 1. The region was chosen to be in the coronal hole and not to contain any bright-point emission. Although the jet emission peaks later than the bright-point emission, it began rising at a similar time to the bright point, suggesting that plasma was ejected from very early in the event. Note that in Section 4 a small jet from the initial kernel was identified as early as 08:51:56 UT. The vertical lines indicate the time period when EIS scanned the jet, and it can be seen that the emission had already decayed significantly at this time.

Inspection of images formed in different EIS emission lines suggests that the jet had a rather narrow temperature structure, consistent with the AIA images. An image formed in Fe XI 188.2 Å is similar to that of Fe XII 195.1 Å but Fe XIII 202.0 Å shows a much weaker signature. Fe IX 197.9 Å and Fe X 184.5 Å images show emission in the lower part of the jet, *i.e.*  $y$ -values of  $-520$  to  $-560$  in Figure 1. He II 256.3 Å and O V 192.9 Å show some emission just above the bright point, but no obvious emission within the main body of the jet.

The Fe XII 195.12 Å emission line profiles in the jet clearly demonstrate a two component structure, which we interpret as a superposition of the jet plasma and the background coronal hole plasma. For this reason a two-Gaussian fit was applied to the line profile, and Figure 7 shows the results. The intensity and velocity maps for the “background” component are shown in panels 7a and 7b. The bright point that is the source of the jet is seen in the top-left corner of the intensity image. (A much larger and more intense bright point, not related to the jet, is seen at the bottom of the image.) The velocity image for the background component is scaled between  $-15 \text{ km s}^{-1}$  and  $+15 \text{ km s}^{-1}$  and weak blueshifts are seen above the bright point. Panels 7c and 7d show the intensity and velocity maps for the “jet” Gaussian component. Where reliable two Gaussian fits were not possible, these pixels are white in the two images. It can be seen that the second component is present mainly in the thick columnar structure previously highlighted in Figure 1. This demonstrates that the enhanced line width seen in the single Gaussian fit is actually due to the presence of an extra Gaussian component.

Crosses on panels 7c and 7d indicate the spatial locations for which the line profiles in panels 7e–g were extracted. For locations in the column that are closer to the bright point, the jet velocity is smaller and so the line profile has the appearance of a single broad line (panel 7e). For locations further from the bright point, the two Gaussian components are clearly separated (panels 7f and 7g). A histogram showing all of the jet velocities is shown in panel 7h. The distribution has a mean of  $-173 \text{ km s}^{-1}$  and a standard deviation of  $42 \text{ km s}^{-1}$ .

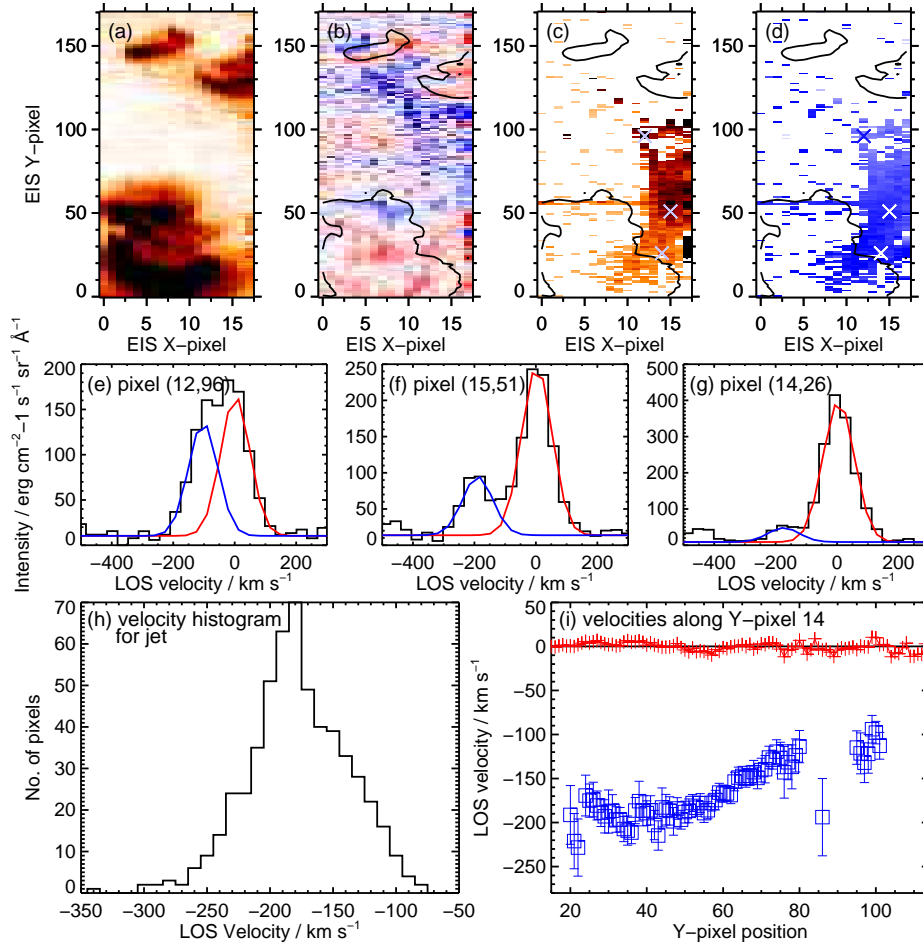


**Figure 7.** Results from the two Gaussian fit to the EIS Fe XII 195.12 Å emission line. Panels a and c show intensity maps for the two components with a reverse intensity scaling applied, and panel a is saturated at  $100 \text{ erg cm}^{-2} \text{ s}^{-1} \text{ sr}^{-1}$ . Panels b and d show velocity maps. Contours on panels b–d show an intensity level of  $50 \text{ erg cm}^{-2} \text{ s}^{-1} \text{ sr}^{-1}$  from panel a. Crosses on panels c and d indicate the spatial pixels for which the spectra shown in panels e–g were extracted. The red and blue curves in panels e–g show the two Gaussian components. Panel h shows the velocity histogram for the high-velocity jet component extracted from  $x$ -pixels 9 to 17 and  $y$ -pixels 0 to 109. Panel g shows a slice through the two velocity maps (panels b and d) at  $y$ -pixel 14.

Panel 7i shows a slice through the two velocity images (panels 7b and 7d) at  $x$ -pixel 14. This demonstrates that the background component (red) is close to rest velocity while the jet component (blue) increases with distance from the bright point from about  $-100 \text{ km s}^{-1}$  to about  $-200 \text{ km s}^{-1}$ .

This latter finding is important as it implies that the plasma is being accelerated as it travels away from the bright point. Previous authors have noted that jet velocities measured from image sequences are often not sufficient for the plasma to escape from the Sun (Culhane *et al.*, 2007). Spectroscopic velocity

measurements are a more accurate reflection of the true plasma velocity, and the increasing velocity with height found here suggests that jet plasma could escape the Sun even if the velocities reported at low heights are below the escape velocity. The theoretical model of Pariat, Antiochos, and DeVore (2009) demonstrated that nonlinear Alfvén waves can escape along open field lines following magnetic reconnection of twisted, closed magnetic field within the bright point. Such waves could be responsible for accelerating the plasma in the jet.

At the height for which the projected jet velocity was derived from the *A193* data, the EIS LOS velocity is  $\approx 100 \text{ km s}^{-1}$ , so the projected velocity is around a factor two larger than the LOS velocity. The cosine factor at the location of the bright point is 0.77 so for a radial jet one would expect the LOS velocity to be larger than the projected velocity. Therefore, at least at relatively low heights, the jet has a somewhat “flat” trajectory. We caution, however, that the projected velocity is determined by the initial intensity front of the jet at  $\approx 09:02$  UT while the EIS LOS velocity measurement reflects measurements made during the period 09:14–09:18 UT.

Density and temperature can be estimated in the jet by considering additional lines to  $195.12 \text{ \AA}$ ; however for these lines it is not possible to make reliable measurements in individual spatial pixels so it is necessary to bin multiple pixels. We chose a  $4 \times 21$  block of pixels within the jet and used the IDL routine `EIS_MASK_SPECTRUM` to create the averaged spectrum; this routine corrects for spatial offsets between different wavelengths.  $\text{Fe XII } 186.9 \text{ \AA}/195.12 \text{ \AA}$  is a good density diagnostic (Young *et al.*, 2007 and Young *et al.*, 2009), and the  $186.9 \text{ \AA}$  profile shows a weak, blueshifted component that can be identified with the jet. Using atomic data from version 7.1 of the CHIANTI database (Dere *et al.*, 1997; Landi *et al.*, 2013) yields a density of  $\log(N_e[\text{cm}^{-3}]) = 8.44^{+0.29}_{-0.39}$  for the weak blue-shifted component corresponding to the jet plasma. Selecting a dark region directly to the East of the jet, we find a density of  $\log(N_e[\text{cm}^{-3}]) = 8.67 \pm 0.05$  thus the jet density is consistent with this value, *i.e.* the jet does not show any significant density increase over the background coronal hole. The average intensity measured in the jet is  $5.2 \text{ erg cm}^{-2} \text{ s}^{-1} \text{ sr}^{-1}$  so converting to a column depth yields a value of 1300 km, much smaller than the observed width of the jet. This suggests that a curtain is an apt description of the jet, it being much thinner in the line-of-sight direction than in the plane of the sky.

An additional jet component to the background component can only be clearly identified for the two  $\text{Fe XII}$  lines discussed in the previous paragraph and  $\text{Fe XI } 188.22 \text{ \AA}$  and  $\text{Fe XIII } 202.04 \text{ \AA}$ . Again using atomic data from CHIANTI, the  $\text{Fe XIII } 202.04 \text{ \AA}/\text{Fe XII } 195.12 \text{ \AA}$  and  $\text{Fe XII } 195.12 \text{ \AA}/\text{Fe XI } 188.22 \text{ \AA}$  ratios yield isothermal temperatures of  $\log T = 6.16$  and  $6.12$ , respectively, so we can say that the ejected plasma has a temperature of  $\approx 1.4 \text{ MK}$ .

## 6. Summary

A jet observed in the south coronal hole at 9 February 2011 09:00 UT is identified as a blowout jet based on the disruption of the base arch of the bright point and the ejection of cool plasma during the event. The combination of high-cadence coronal imaging from AIA and XRT, magnetograms from HMI and

coronal spectroscopy from EIS give important new insights into the processes of blowout jets. The key results are:

- The jet has a lifetime of  $\approx 30$  minutes and occurs during a magnetic cancellation event within a small coronal bright point. The cancellation occurs over a period of four hours and ultimately leads to the disappearance of the bright point.
- Photospheric flows derived through local correlation tracking show that the bright point lies in a region of converging flow.
- The bright point shows a number of bright kernels typically of size 1000 km. Lifetimes range from 1 to 15 minutes and brightness variations occur on scales of tens of seconds. The kernels are spatially located close to the minority polarity features of the bright point, and they have temperatures of 1–3 MK.
- Jet emission appears immediately after activity begins in the bright point, although the peak jet emission occurs five minutes after the peak bright point emission. The jet continues to be enhanced over the coronal background ten minutes after the bright point becomes quiescent.
- A loop of cool plasma (a mini-filament?) is ejected during the event and there is evidence that the loop was present in the bright point prior to the jet.
- The jet plasma shows outflowing plasma with LOS speeds of  $100 - 250 \text{ km s}^{-1}$  (with an average value of  $173 \text{ km s}^{-1}$ ), a density of  $2.8 \times 10^8 \text{ cm}^{-3}$ , and a temperature of 1.4 MK.
- The LOS velocity increases along the jet, from  $100 \text{ km s}^{-1}$  to  $250 \text{ km s}^{-1}$  suggesting that the plasma is being accelerated within the jet, not just at the bright point.

**Acknowledgment** The authors acknowledge funding from National Science Foundation grant AGS-1159353. Valuable comments from the anonymous referee and E. Pariat are acknowledged. SDO is a mission for NASA’s Living With a Star program. Data are provided courtesy of NASA/SDO and the AIA and HMI science teams. *Hinode* is a Japanese mission developed and launched by ISAS/JAXA, with NAOJ as domestic partner and NASA and STFC (UK) as international partners. It is operated by these agencies in co-operation with ESA and NSC (Norway).

## References

- Boerner, P., Edwards, C., Lemen, J., Rausch, A., Schrijver, C., Shine, R., Shing, L., Stern, R., Tarbell, T., Title, A., Wolfson, C.J., Soufi, R., Spiller, E., Gullikson, E., McKenzie, D., Windt, D., Golub, L., Podgorski, W., Testa, P., Weber, M.: 2012, Initial Calibration of the Atmospheric Imaging Assembly (AIA) on the Solar Dynamics Observatory (SDO). *Solar Phys.* **275**, 41. DOI. ADS.
- Chifor, C., Isobe, H., Mason, H.E., Hannah, I.G., Young, P.R., Del Zanna, G., Krucker, S., Ichimoto, K., Katsukawa, Y., Yokoyama, T.: 2008, Magnetic flux cancellation associated with a recurring solar jet observed with *Hinode*, *RHESSI*, and *STEREO/EUVI*. *Astron. Astrophys.* **491**, 279. DOI. ADS.



- Culhane, J.L., Harra, L.K., James, A.M., Al-Janabi, K., Bradley, L.J., Chaudry, R.A., Rees, K., Tandy, J.A., Thomas, P., Whillock, M.C.R., Winter, B., Doschek, G.A., Korendyke, C.M., Brown, C.M., Myers, S., Mariska, J., Seely, J., Lang, J., Kent, B.J., Shaughnessy, B.M., Young, P.R., Simnett, G.M., Castelli, C.M., Mahmoud, S., Mapson-Menard, H., Probyn, B.J., Thomas, R.J., Davila, J., Dere, K., Windt, D., Shea, J., Hagood, R., Moye, R., Hara, H., Watanabe, T., Matsuzaki, K., Kosugi, T., Hansteen, V., Wikstol, Ø.: 2007, The EUV Imaging Spectrometer for Hinode. *Solar Phys.* **243**, 19. DOI. ADS.
- Dere, K.P., Landi, E., Mason, H.E., Monsignor Fossi, B.C., Young, P.R.: 1997, CHIANTI - an atomic database for emission lines. *Astron. Astrophys. Supp. Ser.* **125**, 149. DOI. ADS.
- Doschek, G.A., Landi, E., Warren, H.P., Harra, L.K.: 2010, Bright Points and Jets in Polar Coronal Holes Observed by the Extreme-Ultraviolet Imaging Spectrometer on Hinode. *Astrophys. J.* **710**, 1806. DOI. ADS.
- Fisher, G.H., Welsch, B.T.: 2008, FLCT: A Fast, Efficient Method for Performing Local Correlation Tracking. In: Howe, R., Komm, R.W., Balasubramaniam, K.S., Petrie, G.J.D. (eds.) *Subsurface and Atmospheric Influences on Solar Activity*, **CS-383**, Astron. Soc. Pac., 373. ADS.
- Golub, L., Deluca, E., Austin, G., Bookbinder, J., Caldwell, D., Cheimets, P., Cirtain, J., Cosmo, M., Reid, P., Sette, A., Weber, M., Sakao, T., Kano, R., Shibasaki, K., Hara, H., Tsuneta, S., Kumagai, K., Tamura, T., Shimojo, M., McCracken, J., Carpenter, J., Haight, H., Siler, R., Wright, E., Tucker, J., Rutledge, H., Barbera, M., Peres, G., Varisco, S.: 2007, The X-Ray Telescope (XRT) for the Hinode Mission. *Solar Phys.* **243**, 63. DOI. ADS.
- Hannah, I.G., Kontar, E.P.: 2012, Differential emission measures from the regularized inversion of Hinode and SDO data. *Astron. Astrophys.* **539**, A146. DOI. ADS.
- Huang, Z., Madjarska, M.S., Doyle, J.G., Lamb, D.A.: 2012, Coronal hole boundaries at small scales. IV. SOT view. Magnetic field properties of small-scale transient brightenings in coronal holes. *Astron. Astrophys.* **548**, A62. DOI. ADS.
- Kamio, S., Hara, H., Watanabe, T., Matsuzaki, K., Shibata, K., Culhane, L., Warren, H.P.: 2007, Velocity Structure of Jets in a Coronal Hole. *Pub. Astron. Soc. Japan* **59**, 757. ADS.
- Kamio, S., Hara, H., Watanabe, T., Curdt, W.: 2009, Distribution of jets and magnetic fields in a coronal hole. *Astron. Astrophys.* **502**, 345. DOI. ADS.
- Kosugi, T., Matsuzaki, K., Sakao, T., Shimizu, T., Sone, Y., Tachikawa, S., Hashimoto, T., Minesugi, K., Ohnishi, A., Yamada, T., Tsuneta, S., Hara, H., Ichimoto, K., Suematsu, Y., Shimojo, M., Watanabe, T., Shimada, S., Davis, J.M., Hill, L.D., Owens, J.K., Title, A.M., Culhane, J.L., Harra, L.K., Doschek, G.A., Golub, L.: 2007, The Hinode (Solar-B) Mission: An Overview. *Solar Phys.* **243**, 3. DOI. ADS.
- Landi, E., Young, P.R., Dere, K.P., Del Zanna, G., Mason, H.E.: 2013, CHIANTI—An Atomic Database for Emission Lines. XIII. Soft X-Ray Improvements and Other Changes. *Astrophys. J.* **763**, 86. DOI. ADS.
- Lemen, J.R., Title, A.M., Akin, D.J., Boerner, P.F., Chou, C., Drake, J.F., Duncan, D.W., Edwards, C.G., Friedlaender, F.M., Heyman, G.F., Hurlburt, N.E., Katz, N.L., Kushner, G.D., Levay, M., Lindgren, R.W., Mathur, D.P., McFeaters, E.L., Mitchell, S., Rehse, R.A., Schrijver, C.J., Springer, L.A., Stern, R.A., Tarbell, T.D., Wuelser, J.-P., Wolfson, C.J., Yanari, C., Bookbinder, J.A., Cheimets, P.N., Caldwell, D., Deluca, E.E., Gates, R., Golub, L., Park, S., Podgorski, W.A., Bush, R.I., Scherrer, P.H., Gumm, M.A., Smith, P., Aufer, G., Jerram, P., Pool, P., Soufli, R., Windt, D.L., Beardsley, S., Clapp, M., Lang, J., Waltham, N.: 2012, The Atmospheric Imaging Assembly (AIA) on the Solar Dynamics Observatory (SDO). *Solar Phys.* **275**, 17. DOI. ADS.
- Liu, C., Deng, N., Liu, R., Ugarte-Urra, I., Wang, S., Wang, H.: 2011, A Standard-to-blowout Jet. *Astrophys. J. Lett.* **735**, L18. DOI. ADS.
- Liu, Y., Scherrer, P.H., Hoeksema, J.T., Schou, J., Bai, T., Beck, J.G., Bobra, M., Bogart, R.S., Bush, R.I., Couvidat, S., Hayashi, K., Kosovichev, A.G., Larson, T.P., Rabello-Soares, C., Sun, X., Wächter, R., Zhao, J., Zhao, X.P., Duvall, T.L. Jr., DeRosa, M.L., Schrijver, C.J., Title, A.M., Centeno, R., Tomczyk, S., Borrero, J.M., Norton, A.A., Barnes, G., Crouch, A.D., Leka, K.D., Abnett, W.P., Fisher, G.H., Welsch, B.T., Muglach, K., Schuck, P.W., Wiegmann, T., Turmon, M., Linker, J.A., Mikić, Z., Riley, P., Wu, S.T.: 2012, A First Look at Magnetic Field Data Products from SDO/HMI. In: Bellot Rubio, L., Reale, F., Carlsson, M. (eds.) *4th Hinode Science Meeting: Unsolved Problems and Recent Insights*, **CS-455**, Astron. Soc. Pac., 337. ADS.
- Madjarska, M.S.: 2011, Dynamics and plasma properties of an X-ray jet from SUMER, EIS, XRT, and EUVI A & B simultaneous observations. *Astron. Astrophys.* **526**, A19. DOI. ADS.

- Moore, R.L., Cirtain, J.W., Sterling, A.C., Falconer, D.A.: 2010, Dichotomy of Solar Coronal Jets: Standard Jets and Blowout Jets. *Astrophys. J.* **720**, 757. DOI. ADS.
- Moreno-Insartís, F., Galsgaard, K.: 2013, Plasma Jets and Eruptions in Solar Coronal Holes: A Three-dimensional Flux Emergence Experiment. *Astrophys. J.* **771**, 20. DOI. ADS.
- Muglach, K.: 2008, Explosive Events and the Evolution of the Photospheric Magnetic Field. *Astrophys. J.* **687**, 1398. DOI. ADS.
- Nisticò, G., Bothmer, V., Patsourakos, S., Zimbardo, G.: 2009, Characteristics of EUV Coronal Jets Observed with STEREO/SECCHI. *Solar Phys.* **259**, 87. DOI. ADS.
- O’Dwyer, B., Del Zanna, G., Mason, H.E., Weber, M.A., Tripathi, D.: 2010, SDO/AIA response to coronal hole, quiet Sun, active region, and flare plasma. *Astron. Astrophys.* **521**, A21. DOI. ADS.
- Pariat, E., Antiochos, S.K., DeVore, C.R.: 2009, A Model for Solar Polar Jets. *Astrophys. J.* **691**, 61. DOI. ADS.
- Reeves, K.K., Gibson, S.E., Kucera, T.A., Hudson, H.S., Kano, R.: 2012, Thermal Properties of a Solar Coronal Cavity Observed with the X-Ray Telescope on Hinode. *Astrophys. J.* **746**, 146. DOI. ADS.
- Scherrer, P.H., Schou, J., Bush, R.I., Kosovichev, A.G., Bogart, R.S., Hoeksema, J.T., Liu, Y., Duvall, T.L., Zhao, J., Title, A.M., Schrijver, C.J., Tarbell, T.D., Tomczyk, S.: 2012, The Helioseismic and Magnetic Imager (HMI) Investigation for the Solar Dynamics Observatory (SDO). *Solar Phys.* **275**, 207. DOI. ADS.
- Tsuneta, S., Ichimoto, K., Katsukawa, Y., Nagata, S., Otsubo, M., Shimizu, T., Suematsu, Y., Nakagiri, M., Noguchi, M., Tarbell, T., Title, A., Shine, R., Rosenberg, W., Hoffmann, C., Jurcevich, B., Kushner, G., Levay, M., Lites, B., Elmore, D., Matsushita, T., Kawaguchi, N., Saito, H., Mikami, I., Hill, L.D., Owens, J.K.: 2008, The Solar Optical Telescope for the Hinode Mission: An Overview. *Solar Phys.* **249**, 167–196. DOI. ADS.
- Wang, H., Johannesson, A., Stage, M., Lee, C., Zirin, H.: 1998, Study of HA Jets on the Quiet Sun. *Solar Phys.* **178**, 55. DOI. ADS.
- Yang, S., Zhang, J., Li, T., Liu, Y.: 2011, SDO Observations of Magnetic Reconnection At Coronal Hole Boundaries. *Astrophys. J. Lett.* **732**, L7. DOI. ADS.
- Young, P.R.: 2012, EIS\_AUTO\_FIT and SPEC\_GAUSS\_EIS: Gaussian fitting routines for the Hinode/EIS mission. *EIS Software Note No. 16, ver. 2.4.* [ftp://sohftp.nascom.nasa.gov/solarsoft/hinode/eis/doc/eis\\_notes/07\\_LINE\\_WIDTH/eis\\_swnote\\_07.pdf](ftp://sohftp.nascom.nasa.gov/solarsoft/hinode/eis/doc/eis_notes/07_LINE_WIDTH/eis_swnote_07.pdf)
- Young, P.R., Del Zanna, G., Mason, H.E., Dere, K.P., Landi, E., Landini, M., Doschek, G.A., Brown, C.M., Culhane, L., Harra, L.K., Watanabe, T., Hara, H.: 2007, EUV Emission Lines and Diagnostics Observed with Hinode/EIS. *Pub. Astron. Soc. Japan* **59**, 857. ADS.
- Young, P.R., Watanabe, T., Hara, H., Mariska, J.T.: 2009, High-precision density measurements in the solar corona. I. Analysis methods and results for Fe XII and Fe XIII. *Astron. Astrophys.* **495**, 587. DOI. ADS.
- Young, P.R., Doschek, G.A., Warren, H.P., Hara, H.: 2013, Properties of a Solar Flare Kernel Observed by Hinode and SDO. *Astrophys. J.* **766**, 127. DOI. ADS.

## Appendix

### A. AIA DEM Analysis of Bright Point Kernels

A differential emission measure analysis of two of the bright point kernels was attempted using the AIA filter data, but the results are not considered accurate due to the large emission measure found at  $\approx 10^7$  K, which is inconsistent with the XRT filter ratio results. Here we record the method used to derive the AIA DEM curves.

The multiple filters of AIA give access to a wide range of temperatures; however for most of the channels the temperature response functions show multiple peaks due to emission lines formed at different temperatures contributing to the passband (Boerner *et al.*, 2012). Hannah and Kontar (2012) presented a

**Table 1.** Kernel intensity measurements.

| Kernel | Intensity / DN s <sup>-1</sup> |     |      |      |      |     |
|--------|--------------------------------|-----|------|------|------|-----|
|        | 94                             | 131 | 171  | 193  | 211  | 335 |
| 1      | 64                             | 769 | 8791 | 4995 | 1420 | 89  |
| 2      | 8                              | 50  | 703  | 929  | 278  | 14  |

differential emission measure method that can be applied to AIA data, and this was applied to the initial kernel using images obtained between 08:51:49 and 08:51:59 UT, and also a bright elongated feature observed between 09:02:26 and 09:02:37 UT (Figure 5g) that probably consists of two or three kernels. We refer to these two features as “kernel 1” and “kernel 2”, respectively. The kernel intensities for the six coronal filters, *A94*, *A131*, *A171*, *A193*, *A211*, and *A335*, were measured and a background intensity was subtracted for each of the *A131*, *A171*, *A193*, and *A211* filters (the background level for the remaining filters was negligible). The values are given in Table 1. The Hannah and Kontar (2012) method yielded a continuous DEM curve between  $\log T = 5.6$  and 7.4 for each kernel and they are shown in Figure 8. (We note that the `/noblend`, `/evenorm`, and `/chiantifix` keywords were applied when retrieving the AIA response functions.) Both curves show emission at low temperatures ( $\log T = 5.9$  to 6.4) with a further peak at  $\log T = 7.1$ , suggesting there is a significant amount of very hot plasma in the kernels. However, this result is at odds with the XRT observations, since both the Ti-poly and Be-thin filters are much more sensitive at  $10^7$  K than  $10^6$  K. Folding the XRT response curves with the derived DEMs yields predicted Be-thin/Ti-poly ratios of 0.68 and 0.66 for the two kernels, much higher than the measured ratios during the XRT sequence. The reason for the spurious DEM curves from AIA is likely due to contributions of cool lines to the *A94* and *A131* channels that are currently unaccounted for in atomic models.

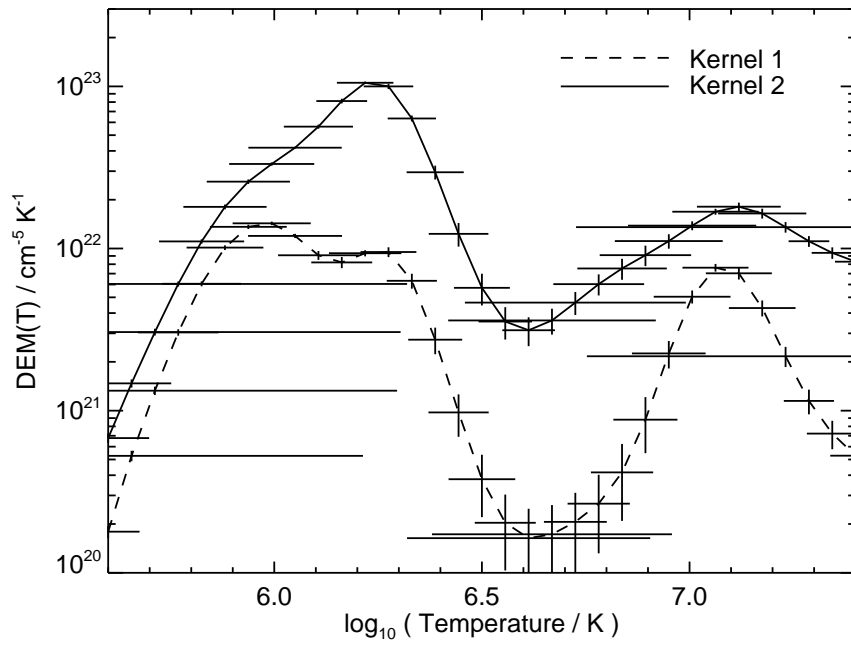


**Figure 8.** Differential emission measure curves for two kernels within the jet bright point, derived from AIA filter intensities.